Advanced Functional Materials

ADVANCED FUNCTIONAL MATERIALS
www.afm-journal.de

RESEARCH ARTICLE OPEN ACCESS

Inducing Ferromagnetism by Structural Engineering in a Strongly Spin-Orbit Coupled Oxide

Ji Soo Lim[1] | Carmine Autieri[2,3] | Merit Spring[1] | Martin Kamp[1] | Amar Fakhredine[4] | Pavel Potapov[5] | Daniel Wolf[5] | Sergii Pylypenko[5] | Axel Lubk[5,6] | Johannes Schultz[5] | Nicolas Perez[5] | Börge Mehlhorn[5,6] | Louis Veyrat[7] | Mario Cuoco[3] | Fadi Choueikan[8] | Philippe Ohresser[8] | Bernd Büchner[5,6] | Giorgio Sangiovanni[9] | Ralph Claessen[1] | Michael Sing[1]

[1]Physikalisches Institut and Würzburg-Dresden Cluster of Excellence ct.Qmat, Universität Würzburg, Würzburg, Germany | [2]International Research Centre MagTop, Institute of Physics, Polish Academy of Sciences, Warsaw, Poland | [3]CNR-SPIN, UOS Salerno, Fisciano, Italy | [4]Institute of Physics, Polish Academy of Sciences, Warsaw, Poland | [5]Leibniz Institute for Solid State and Materials Research Dresden and Würzburg-Dresden Cluster of Excellence ct.Qmat, Dresden, Germany | [6]Institute of Solid State and Materials Physics and Würzburg- Dresden Cluster of Excellence ct.Qmat, TU Dresden, Dresden, Germany | [7]CNRS, Laboratoire National des Champs Magnétiques Intenses, Université Grenoble-Alpes, Université Toulouse 3, INSA-Toulouse, EMFL, Toulouse, France | [8]Synchrotron SOLEIL, Saint-Aubin, France | [9]Institut Für Theoretische Physik Und Astrophysik and Würzburg-Dresden Cluster of Excellence ct.Qmat, Universität Würzburg, Würzburg, Germany

Correspondence: Ji Soo Lim (ji.lim@kit.edu) | Carmine Autieri (autieri@magtop.ifpan.edu.pl) | Michael Sing (michael.sing@uni-wuerzburg.de)

Received: 26 January 2026 | **Accepted:** 30 January 2026

Keywords: anomalous hall effect | face-shared octahedra | iridate | spin-orbit coupling | stoner ferromagnetism | X-ray magnetic circular dichroism

ABSTRACT

Magnetic materials with strong spin-orbit coupling (SOC) are essential for the advancement of spin-orbitronic devices, as they enable efficient spin-charge conversion, complex magnetic structures, spin-valley physics, topological phases and other exotic phenomena. 5d transition-metal oxides such as $SrIrO_3$ feature large SOC, but usually show paramagnetic behavior due to broad bands and a low density of states at the Fermi level, accompanied by a relatively low Coulomb repulsion. Here, we unveil ferromagnetism in 5d $SrIrO_3$ thin films grown on $SrTiO_3$ (111). Through substrate-induced structural engineering, a zigzag stacking of three-unit-cell thick layers along the [111] direction is achieved, stabilizing a ferromagnetic state at the interfaces. Magnetotransport measurements reveal an anomalous Hall effect below ~30 K and hysteresis in the Hall conductivity below 7 K, indicating ferromagnetic ordering. X-ray magnetic circular dichroism further supports these results. Theoretical analysis suggests that the structural engineering of the IrO_6 octahedral network enhances the density of states at the Fermi level and thus stabilizes Stoner ferromagnetism. This work highlights the potential of structurally engineered 5d oxides for spin-orbitronic devices, where efficient control of SOC-induced magnetic phases by electric currents can lead to lower energy consumption and improved performance in next-generation device technologies.

1 | Introduction

Magnetic materials play a crucial role in current information-processing devices such as hard disks and magnetic random-access memories (MRAMs), and they are actively being developed for future spin-orbitronic devices [1–6]. In particular, there has been a growing interest in controlling the direction of magnetization using electric currents, as this offers significant potential

Ji Soo Lim and Carmine Autieri contributed equally to this work.

for novel devices with low energy consumption [7–9]. A key factor for the realization of efficient spin-charge conversion is the presence of strong spin-orbit coupling (SOC), which increases the spin Hall angle and generates larger spin currents [10]. Ferromagnetic materials with strong SOC allow a perpendicular magnetic moment to be efficiently switched by an in-plane current flow without an external magnetic field [11–13].

To achieve a large SOC, materials containing 4d or 5d heavy elements are usually required. However, these elements have extended orbitals, which lead to a delocalization of electrons that weakens electron-electron correlations and often results in paramagnetic behavior. Aside from conventional exchange interactions, ferromagnetism in such systems can also arise from satisfying the Stoner instability criterion, as exemplified by $SrRuO_3$ – a well-known 4d itinerant ferromagnet [14, 15]. Recently, it has been shown that applying an electric current can change its out-of-plane magnetization direction in thin films with (001)-orientation [16]. These findings highlight the importance of designing ferromagnetic materials with strong SOC for spin-orbitronic device applications.

Here, we report the emergence of ferromagnetism in thin films of 5d $SrIrO_3$ (SIO) with a d^5 electron configuration when grown with (111)-orientation on $SrTiO_3$. In contrast, epitaxially stabilized (001)-oriented SIO films, which are known to adopt a perovskite structure, exhibit paramagnetic, metallic behavior across various substrates. For instance, 35 nm-thick films grown on $GdScO_3$ (110)—which is nearly lattice-matched to the pseudocubic lattice derived from orthorhombic bulk SIO—were found to remain paramagnetic down to 300 mK [17]. On the other hand, films on $SrTiO_3$ (001) undergo a metal-insulator transition (MIT) at a critical thickness of four unit cells (uc), that is, toward the 2D limit when correlations are enhanced. This may be accompanied by in-plane magnetism arising from canted antiferromagnetic (AFM) ordering, as suggested by density functional theory (DFT) calculations [18, 19]. However, their highly insulating nature would, in any case, limit their suitability for current-driven devices. Signatures of ferromagnetic phases were observed in artificial $[(SrIrO_3)_m, SrTiO_3]$ superlattices, but again only in conjunction with insulating behavior, below $m = 3$ [20], while itinerant ferromagnetism, induced by proximity, was reported in superlattices with the ferromagnetic insulator $LaCoO_3$ [21]. Generally, in d^5 iridates, the large SOC leads to the entanglement of the spin and orbital degrees of freedom, associated with the formation of $J_{eff} = 1/2$ states. This results in a narrow, half-filled band, susceptible to Mott localization and favors superexchange-driven AFM interactions, specifically for corner-sharing octahedra with 180° Ir-O-Ir bond angles. This typically stabilizes a robust antiferromagnetic insulating phase that is difficult to convert into a ferromagnetic state [22, 23].

Given that bulk SIO, which adopts a monoclinic distortion of the hexagonal $BaTiO_3$ structure, is a non-Fermi-liquid metal close to a ferromagnetic instability [24], SIO (111) thin films offer a promising route to stabilize a hexagonal lattice motif and potentially realize intrinsic itinerant ferromagnetism. Also, due to the geometrically frustrated spin configuration in combination with strain, unexpected magnetic states with potential topological characteristics could emerge [25]. Both perspectives highlight SIO (111) films as an intriguing materials platform well worth closer investigation. However, achieving perovskite SIO (111) films is known to be challenging, primarily due to the fact that the bulk monoclinic phase is thermodynamically more stable [26]. Recent studies have demonstrated that *monoclinic* SIO films can be epitaxially grown on STO (111) substrates [27, 28], featuring a thickness-driven transition into a magnetic insulating state [28]. Furthermore, superlattice engineering has been employed to realize a well-defined perovskite structure with (111) orientation. A SIO(6 uc)/STO(4 uc) superlattice exhibits an anomalous Hall effect under both in-plane and out-of-plane magnetic fields, with the magnetic easy axis lying in-plane [29]. While these studies provide intriguing insights into the magnetic state, detailed investigations of the crystal structure and the spin configuration of SIO (111) films are still lacking, and the link between structure and magnetism remains unclear. In this work, we combine structural and magnetotransport measurements with theoretical analysis to shed light on the magnetic properties and their microscopic origin in SIO (111) films.

2 | Results and Discussion

We first explore the structural properties of an SIO (111) film (~ 20 uc thick) grown on STO (111). The thickness of the SIO (111) film, fabricated by pulsed laser deposition, was determined from the reflection high-energy electron diffraction (RHEED) oscillations (see Figure S1a). After finishing the film growth, we carried out in situ low-energy electron diffraction (LEED), exhibiting a sixfold structural symmetry (see Figure S1c). X-ray diffraction shows a single-phase SIO (111) film with a *c*-axis lattice parameter of about 2.40 Å (Figure 1a), which is slightly larger than reported in Ref. [28] ($c = 2.35$ Å≈ 14.12 Å /6) for fully relaxed monoclinic (m-SIO) films of thicknesses between 5.7 nm and 90 nm. The width of the rocking curve of the SIO (111) peak is about 0.15° (see inset of Figure 1a), indicating that the film is of high crystalline quality.

An additional peak between the SIO (111) and (222) reflections, marked as SL+, is positioned at precisely 1.33 r.l.u. (Figure S2b), indicating a three-unit-cell periodicity, which is also seen in the high-angle annular dark field (HAADF) scanning transmission electron microscope (STEM) image in Figure 1b. While an analysis of the TEM images along the [11, 12] zone axis in terms of the tilt angle is not conclusive due to the drift during scanning, the finding of a slightly elongated *c* axis in our films suggests that our thinner films (below 20 uc, i.e., 4.8 nm) may preserve a strained, hexagonal-like structure rather than adopting the relaxed monoclinic form as in Ref. [28]. Although this SL+ peak was previously identified as the (008) reflection of the reported m-SIO, it is denoted as SL+ in this study to distinguish it from the strained superstructure. The strained hexagonal superstructure is presumed to develop from an initial accommodation layer (yellow box in Figure 1b,d). It has been reported that at polar (111) oxide interfaces, the initial growth layer accommodates the interfacial mismatch primarily through local rearrangements of the oxygen sublattice and distortions of the B-site octahedral network [30]. In this context, we hypothesize that the first IrO_3 layer of the SIO (111) film may be locally distorted and partially disordered at the atomic scale. Such atomic-scale disorder can occur without complete strain relaxation. Once this initial accommodation layer is formed, the subsequent layers experience the epitaxial constraint imposed by the STO (111) substrate and thus recover

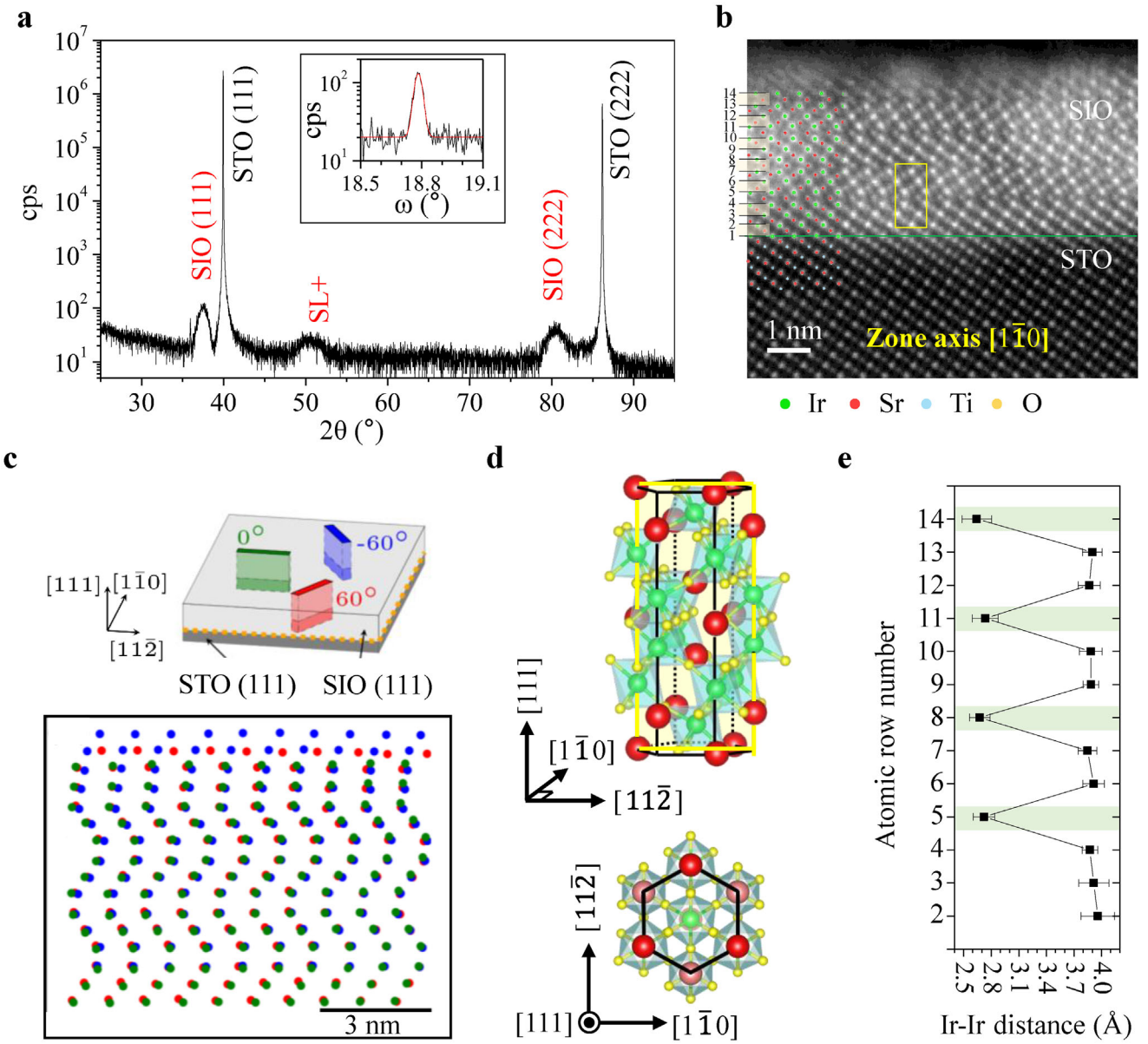

FIGURE 1 | Structural properties of SIO (111) films grown on STO (111) substrates. (a) X-ray diffractogram of a 2θ–ω scan. The inset shows a rocking curve of the SIO (111) diffraction peak. (b), Scanning transmission electron microscopy image along the [1$\bar{1}$0] zone axis. The numbers on the left denote the atomic rows in the image containing Ir atoms, counted from the interface. The yellow box highlights the region discussed in (d). (c), Arrangement of Ir atoms, generated from STEM images along three different zone axes, as illustrated in the schematic above. See Supporting information for details. (c), Arrangement of Ir atoms, generated from STEM images along three different zone axes, as illustrated in the schematic above. See Supporting information for details. (d), 3D hexagonal crystal structure as inferred from the STEM data. The figure below shows a top view of the crystal structure. The lattice vectors are specified in relation to the STO substrate. The yellow box corresponds to the projected atomic configuration in (b). (e), The average Ir-Ir distance in the face-shared (green colored) and the corner-shared (uncolored) octahedra. The atomic row numbers *i* refer to the numbers in (b) with the Ir-Ir distance given for each row being determined from the averaged distances of Ir atoms in this row and the next row *i*-1 to the interface.

the strained hexagonal configuration. Furthermore, the small substrate miscut of less than 0.1° suppresses defect formation and island growth, thereby facilitating the stable growth of strain-preserved SIO (111) films [31].

The in-plane lattice parameter obtained from TEM images along different zone axes, namely [1$\bar{1}$0] and [11$\bar{2}$], shows that the film is well strained to the STO substrate (see Figure S2). To confirm the sixfold structural symmetry from the LEED measurement, we compare STEM images from three other lamellae, cut at different angles as sketched in Figure 1c, top. From these data, we determined the Ir positions with pm-scale precision, which are marked by green, red, and blue dots, corresponding to the lamellae with angles of 0°, −60°, and 60° with respect to the [11$\bar{2}$] axis, respectively (Figure S2d). The Ir atomic positions from the different lamellae coincide well with each other, indicating a sixfold symmetry as seen by LEED (Figure 1c, bottom). This implies that the SIO (111) film shows a hexagonal superstructure. By combining all TEM images, we obtain the 3D crystal structure depicted in Figure 1d. The interface between twinned stacks

exhibits a face-shared octahedral structure, whereas the interior of the stacks consists of corner-shared octahedra as in a perovskite structure. The average distance between Ir-Ir ions in the face-shared octahedral arrangement is determined to be 2.7 Å, whereas in the corner-shared octahedral arrangement, it measures 3.9 Å (Figure 1e).

To explore the electric transport properties, we first investigate the sheet resistance of SIO (111) films of different thicknesses using van-der-Pauw geometry (see Figure 2a; Figure S3a with a reduced sheet resistance range for better discernibility of the curves). The SIO (111) films exhibit a thickness-dependent MIT at a critical thickness of 5 uc. Below this critical thickness, the SIO (111) films only feature corner-shared octahedra and display insulating behavior. On the other hand, the SIO (111) films above the critical thickness begin to show a zigzag atomic arrangement and the formation of corresponding interfaces with face-shared octahedra. The interactions between these face-shared and the corner-shared octahedra are expected to alter the film's electronic band structure, likely contributing to its metallic behavior. Above the critical thickness, the films display a metal-insulator crossover upon cooling, with the crossover temperature decreasing with increasing thickness and reaching about 50 K for thicknesses above 12 uc (Figure S3b).

As a representative system for a strained and highly conducting sample, we choose a 9 uc thick SIO (111) film comprising two interfaces with face-shared octahedra to exemplarily study its magnetoelectric transport properties $R(B)/R(0)$ (Figure 2b), where $R(B)$ and $R(0)$ are the sheet resistances at a finite B-field and without B-field, respectively. The sudden drop near B = 0 at 2 K may partly originate from magnetoelastic effects. An applied magnetic field can realign domains and induce magnetostrictive strain, which modifies magnetic anisotropy and transiently lowers the resistance [32]. With increasing field, relaxation of the accumulated strain may cause a partial recovery of resistance.

In order to gain a deeper understanding into the relative strengths of SOC and electron–electron correlations, we fit the magneto-conductance data below 10 K using the Maekawa–Fukuyama (MF) formula (Figure 2c) [18]:

$$\frac{\Delta\sigma(B)}{\sigma_0} = -\Psi\left(\frac{1}{2}+\frac{B_e}{B}\right)+\frac{3}{2}\Psi\left(\frac{1}{2}+\frac{B_\varphi+B_{SO}}{B}\right)-\frac{1}{2}\Psi\left(\frac{1}{2}+\frac{B_\varphi}{B}\right) - \left[ln\left(\frac{B_\varphi+B_{SO}}{B_e}\right)+\frac{1}{2}\left(\frac{B_\varphi+B_{SO}}{B_\varphi}\right)\right]-A_K\frac{\sigma(0)}{\sigma_0}B^2$$

where Ψ is the digamma function, $\sigma_0 = e^2/\pi h$is the quantum conductance, and the parameters B_e, B_φ and B_{SO} are the magnetic fields associated with the elastic, inelastic, and spin–orbit relaxation lengths, respectively.B_φ and B_{SO} are obtained from transport measurements and related to the relaxation lengths l_φ and l_{SO} via $B_\varphi = \hbar/4el_\varphi^2$ and $B_{SO} = \hbar/4el_{SO}^2$. The last term is included for considering a classical Drude contribution to the magnetoconductance with the Kohler coefficient A_K, which scales quadratically with the mobility [33]. B_e can be expressed as $B_e = \hbar/4el_e^2$, where the elastic length, l_e, is given by $l_e = \hbar\sigma(3\pi^2 n)^{1/3}/ne^2$ and n is the carrier density. Since SIO can host both holes and electrons, it is difficult to directly determine the total carrier concentration. However, by comparing the fitting errors for various B_e values, we find that the best fit is obtained for $B_e = 1.4$. This value is comparable to the previously reported $B_e = 1.2$ for SIO (001) films (Figure S4).

In Figure 2d we show the inelastic and spin-orbit relaxation lengths as obtained from the fit analysis. The spin–orbit relaxation length, l_{SO}, remains nearly temperature independent because it is governed by elastic scattering processes arising from the intrinsic spin–orbit coupling and the static scattering potential landscape, such as lattice potential, impurities, or interface roughness [34]. These factors are weakly affected by temperature. From the fitting analysis, we find l_{SO} ~25 nm, a value slightly larger than that of SIO (001) (~20 nm). The l_{SO} value of SIO (111) is comparable to that of Au thin films (~30–50 nm), significantly shorter than that of weak-SOC metals such as Ag (~650 nm), and longer than that of strong-SOC metals such as Pt (~12 nm) [35, 36]. This comparison indicates that SIO (111) exhibits a moderate but substantial spin–orbit coupling strength. The inelastic relaxation length, l_φ, is determined by inelastic scattering processes such as electron–electron and electron–phonon interactions. These inelastic processes destroy the quantum mechanical phase of the electron wavefunction. Therefore, the inelastic relaxation length directly sets the characteristic distance over which coherence is maintained. Furthermore, l_φ exhibits a strong temperature dependence. As the temperature increases, the rates of electron–electron and electron–phonon inelastic scattering are enhanced, leading to a decrease of l_φ. Conversely, at lower temperatures, inelastic processes are suppressed, and the phase coherence length becomes longer [37]. The fact that $l_{SO} > l_\phi$implies that electrons lose their phase coherence before spin–orbit scattering becomes significant, leading to constructive interference along time-reversed paths, a hallmark of weak localization. When a magnetic field is applied, this interference is suppressed, resulting in negative magnetoresistance. Since SOC is relatively weak in this regime, the spin–orbit–induced Berry curvature ($\Omega \propto \lambda^2/(E_m - E_n)^2$) and its contribution to the anomalous Hall effect are reduced, suggesting that magnetism becomes relevant for the observed Hall response.

The magnetoresistance $(R_{9T} - R_{0T})/R_{0T}$, plotted in Figure 2e, shows a sudden change from an increasing to a decreasing behavior approximately at 20 K and a sign change from negative to positive at about 7 K. Below 7 K, in the low B-field regime (below ~ 1 T), in addition, a hysteresis loop appears, a typical hallmark of magnetic materials. If ferromagnetic domains in the SIO (111) films align with the field, the reduction of magnetic fluctuations/magnons when approaching saturation can lead to a negative magnetoresistance, as for instance in magnetic 3D topological insulators [38–40]. As the field increases and the magnetization saturates, a further increase in the field's strength leads to orbital effects caused by the Lorentz force, which bends the paths of charge carriers and increases scattering, thereby increasing the resistance [38]. This results in a crossover to positive MR at high magnetic fields, which is observable even at 2 K in a sufficiently strong field of 14 T (Figure S7a). Noticeably, a comparison between the magnetoresistance of SIO (001) and (111) films (see Figure 2c) reveals that, unlike the (111) films, SIO (001) films consistently exhibit positive MR at fields of ±9 T across the entire temperature range (see Figure S5) [17, 41, 42]. To further explore the electronic carrier properties in SIO (001) and (111)

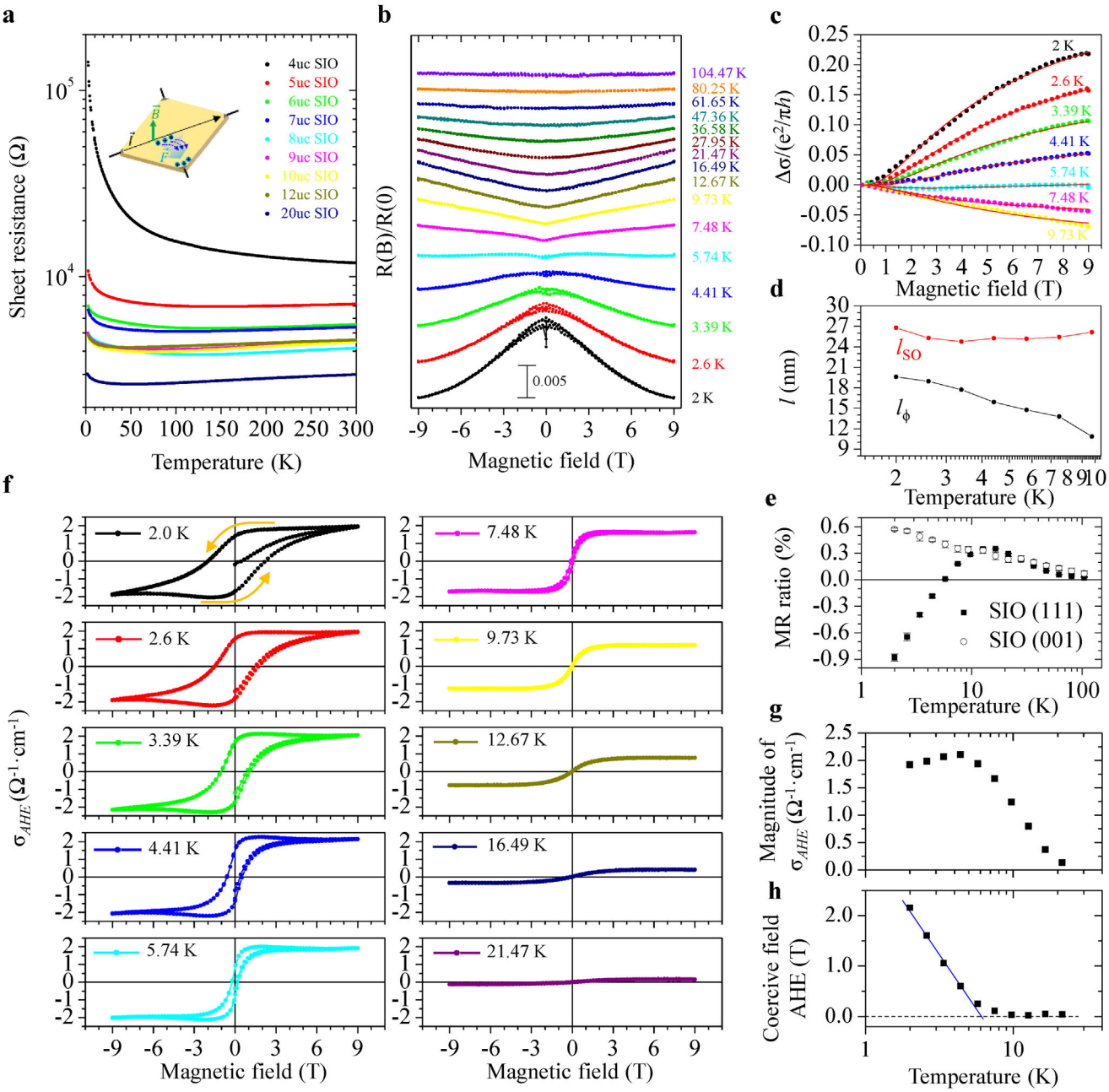

FIGURE 2 | Magnetotransport properties. (a), Temperature-dependent resistance for films with different thicknesses. A metal-insulator transition occurs at 5uc. (b), MR of a 9 uc thick film. (c), Maekawa–Fukuyama formula fitting (red lines) on magnetoconductances. (d), Fitting parameters of l_{SO} and l_{ϕ}. (e), MR ratio of a SIO (001) (empty dots) and a SIO (111) (filled dots) film, with the MR ratio given as a percentage of the average of $(R_{9T} - R_{0T})/R_{0T}$ and $(R_{-9T} - R_{0T})/R_{0T}$. The error bars are calculated from the difference of these two values. (f), Anomalous Hall conductivity, calculated as $\sigma_{AHE} = \rho_{AHE}/(\rho_{AHE}^2 + \rho_{xx}^2)$, of a 9 uc thick film after subtracting the linear component for the ordinary Hall effect. Below about 30 K, the AHE appears and increases with decreasing temperature. Distinct hysteresis loops can be seen below 7 K. (g), Magnitudes of the anomalous Hall conductivity, as obtained from the average of the saturated values $\sigma_{AHE}(6T)$ and $\sigma_{AHE}(-6T)$. (h), Coercive field of the AHE as a function of temperature. Plotted is the average of the magnitudes of the magnetic field at which an anomalous Hall conductivity of zero is observed for each polarity.

films, we conducted anomalous Hall effect (AHE) measurements. Unlike the SIO (001) film, which exhibits linear Hall resistance and electron-dominated transport down to low temperatures, the SIO (111) film shows hole-dominated transport across the entire temperature range (Figure S6). A previous study reported that a 5.7-nm-thick m-SIO film exhibits in-plane magnetization but shows no evidence of an AHE [28]. Our strained SIO (111) films display a clear AHE with pronounced hysteresis at low temperatures under an out-of-plane magnetic field, signifying the emergence of out-ot-plane magnetic moments.

To further analyze the AHE, we isolate its contribution by subtracting a linear component, that is, the ordinary Hall effect, in the region where AHE is observed. We plot the anomalous Hall conductivity in Figure 2f using the equation $\sigma_{AHE} = \rho_{AHE}/(\rho_{AHE}^2 + \rho_{xx}^2)$, where ρ_{AHE} is the transverse resistivity corresponding

to the AHE and ρ_{xx} represents the longitudinal resistivity. The resulting conductivity reaches values up to about 2 $\Omega^{-1}cm^{-1}$, among the highest values reported for oxides and comparable to those in strained pyrochlore iridates such as $Nd_2Ir_2O_7$ [43, 44]. The AHE begins to show hysteresis around 7 K, becoming more pronounced as the temperature decreases. The coercive field of the hysteresis loops scales linearly with the logarithmic temperature (see Figure 2f). This behavior is attributed to ferromagnetic domain motion, where the minimum coercive field required to overcome domain wall pinning is proportional to $\exp[-(\frac{k_BT}{U_i})]$, with k_B and U_i being the Boltzmann constant and the characteristic energy, respectively [45].

The AHE arises from both intrinsic and extrinsic mechanisms: the intrinsic contribution stems from a finite Berry curvature, while the extrinsic part originates from the magnetic scattering of electrons in ferromagnetic materials [46]. In our data, the Hall conductivity exhibits saturation accompanied by hysteresis, consistent with ferromagnetic behavior. Notably, even prior to the onset of hysteresis, the Hall conductivity reaches values close to saturation between 10 and 25 K, suggesting that intrinsic effects contribute to the AHE alongside ferromagnetism.

At high magnetic fields, angle-dependent Hall measurements reveal unusual behavior in the in-plane configuration (Figure S8b,c). While the AHE signal is typically expected to gradually vanish as the magnetic field tilts toward the sample surface, we observe a butterfly-shaped AHE under tilted magnetic fields. This likely results from the saturation field not being reached at the field orientations other than perpendicular to the surface, as it exceeds the maximum experimentally available field of 14 T. Nevertheless, the ferromagnetic-like hysteresis in the AHE under out-of-plane magnetic field indicates ferromagnetic ordering with a preferential out-of-plane magnetic anisotropy.

To independently verify ferromagnetism in SIO (111) films, we performed X-ray magnetic circular dichroism (XMCD) measurements at the Ir M_5 edge ($3d_{5/2} \rightarrow 5f$ or $6p$) in the energy range from 2040 to 2070 eV in normal incidence geometry at the DEIMOS beamline at the SOLEIL synchrotron facility (France) [47]. The 5f orbital has a larger radial extension than the 4f orbital, which results in stronger spatial overlap with the 5d orbital. This suggests that the 5f–5d interaction can be significantly stronger than the 4f–5d interaction. Although no calculations have been reported for Ir, studies have been conducted on typical 5f systems, that is, actinide compounds. For example, in ThO_2 (Th^{4+}, $5f^0$ configuration), 5f and 5d orbitals share the same principal quantum number and have similar radial distributions, leading to substantial orbital overlap [48]. *Ab-initio* Hartree-Fock calculations yield large positive values for the Slater integrals of actinide ions, indicating a strong and positive exchange interaction [49, 50]. As a result, when an electron is excited into an empty 5f orbital, when its spin is parallel to the spin-polarized 5d valence electrons, the total energy of the system is lowered. Conversely, antiparallel spin alignment is resulting in a higher energy state.

Based on this, XMCD at the Ir M_5 edge provides evidence of magnetism. Owing to the limited studies on XMCD at the Ir M edges and the lack of established sum rules, a quantitative estimation of the magnetic moment is not possible. However, in Figure 3a, we plot the absorption spectra for left- and right-circularly polarized light recorded at 5 K and 6 T, which only show subtle differences, indicating tiny magnetic moments, oriented perpendicular to the SIO (111) film surface. As shown in Figure 3b, the XMCD signals for + 6 T and −6 T are inverted relative to each other, which indicates that the magnetic moments align with the external field and change direction when the magnetic field is reversed. The normalized XMCD areas can be regarded as a measure of the magnetization. When plotted as a function of magnetic field over a cycle from −6 T to +6 T and back (see Figure 3c; Figure S8, for the XMCD signals), a hysteresis-like loop as a characteristic of ferromagnetism is obtained. The extracted coercive field is about 0.5 T, which agrees well with the value that can be obtained from Figure 2d at the corresponding temperature.

We further examine the temperature dependence of the normalized XMCD integral, that is, the magnetization, after the SIO (111) film was magnetized at −6T, in zero field, that is, in remanence, starting from 5 K up to 200 K (see Figure 3d). One can clearly see an increase below 50 K (see also Figure S9), supporting that the appearance of MR and AHE approximately below 30 K, as discussed above, is connected to the emergence of a magnetic state. Above 50 K, the XMCD signals and thus the normalized integrals become too weak to be reliably evaluated, with values close to zero. This suggests that the out-of plane magnetization vanishes above this temperature.

To understand the nature and the origin of the ferromagnetic state of the SIO (111) films, we investigated the electronic band structure by DFT calculations including on-site Coulomb repulsion (DFT + U) and X-ray photoelectron spectroscopy (XPS). The crystal structure, which was used as input for the ab initio calculations, was constructed from the analysis of TEM images (Figure 1), with considering spin orientations along the x-, y-, and z-axes. Also, both magnetic and nonmagnetic states were examined to determine the spin configuration with the lowest energy. Our DFT results show that the spins in the ground state are aligned along the z-axis, that is, perpendicular to the surface, consistent with our experimental findings (Figure 4a). The small energy differences between competing magnetic states imply a small transition temperature T_C.

To investigate whether the different structural connectivity of the octahedra in the 3uc thick layers and at their interfaces plays a role in the emergence of magnetism, we performed further analysis. Indeed, the DFT calculations show a higher density of states (DOS) at the Fermi energy E_F associated with the Ir 5d-orbitals for model structures featuring both face- and corner-shared octahedra, as in our films. In contrast, in the case of orthorhombic $SrIrO_3$, which contains solely corner-shared octahedra, a dip at E_F is found, indicative of a bandgap opening caused by strong SOC (Figure 4d). As a result, the latter situation does not fulfill the Stoner criterion and a paramagnetic metal is obtained, whereas in the former case, the larger DOS at E_F does satisfy the Stoner criterion. Moreover, the existence of face-shared octahedra every 3 uc reduces the effective SOC, thereby preventing the system from turning into a Mott insulator [51]. Together, these effects

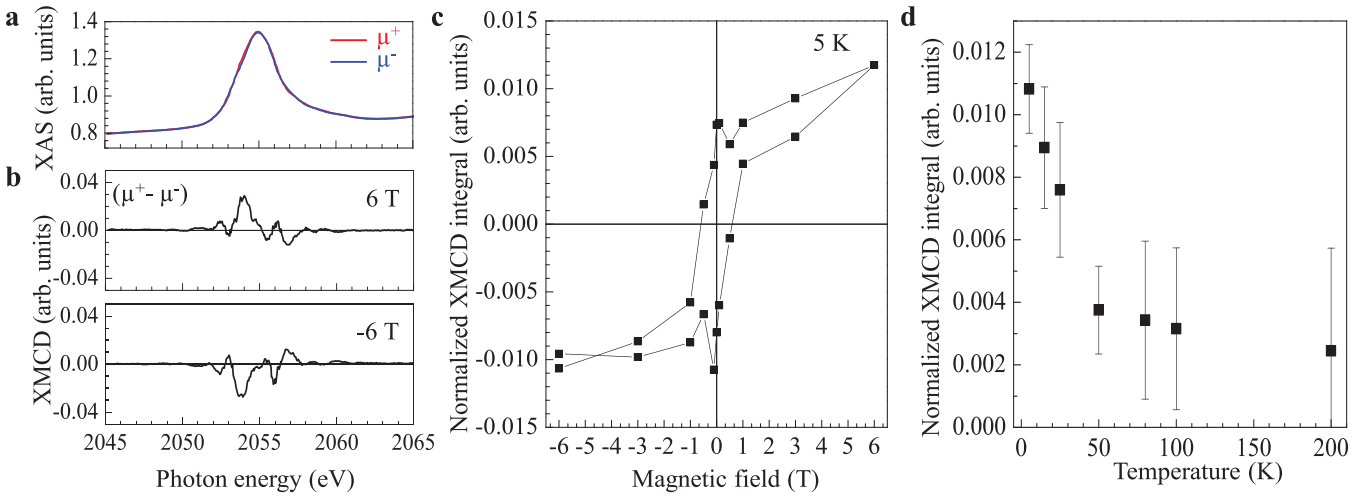

FIGURE 3 | Magnetic properties. (a), X-ray absorption spectroscopy (XAS) spectra at the Ir M_5 edge, measured at 5 K and 6 T with circularly right (red curve, μ^+) and circularly left polarization (blue curve, μ^-). (b), X-ray circular dichroism (XMCD), μ^+—μ^-, at 5 K and magnetic fields of 6 and −6 T. (c), M-H hysteresis loop at 5 K. Each data point represents the integral over the corresponding XMCD signal. (d), XMCD integral as a function of temperature, recorded in remanence after magnetization in a field of −6T. The error bars are estimated from the scatter of repeated measurements.

lead to an itinerant ferromagnetic state, with the DFT calculations yielding a net magnetic moment of 0.03 μ_B/Ir (Figure S10).

Further analysis of the partial density of states associated with the Ir 5d-orbitals reveals that both corner- and face-shared octahedra contribute to the large DOS at E_F, with the dominant contribution arising from the former (Figure 4e). This suggests that primarily the d orbitals of the corner-shared octahedra drive the Stoner instability. On the other hand, the face-shared octahedra play a more significant role in reducing the effective SOC and enabling the structural rearrangement. Additional theoretical results—presented in the Figures S11 and S12 – highlight the presence of semi-Dirac points without magnetization arising from non-symmorphic symmetries, the emergence of Weyl points with finite magnetization that enhance the AHE, and the Fermi surfaces.

To examine the role of face-shared octahedra with respect to the electronic band structure in light of our theoretical findings, we recorded XPS valence band spectra of SIO (001) and (111) films. The SIO (111) film comprises both face- and corner-shared octahedra, while the SIO (001) film consists solely of corner-shared octahedra. Indeed, the Ir 5d derived DOS near E_F is found to be significantly higher for the SIO (111) film (Figure 4b) in good agreement with the theoretical calculations in Figure 4d. In addition, the shorter Ir-Ir distance within the interfaces of face-shared octahedra leads to a stronger orbital overlap than for the corner-shared octahedra and thus a slightly larger bandwidth (Figure 4b). Valence band spectra for SIO (111) films with varying thickness (Figure 4c) confirm this picture. If the thickness is too small for the film to form an interface with face-shared octahedra, that is, at a thickness of 3 uc, the DOS is significantly reduced compared to the films with a thickness of 6 and 9uc. In addition, a MIT with a gap opening occurs, probably due to the electron confinement along the z direction and the associated reduction in the kinetic energy with respect to potential energy due to short-range Coulomb repulsion.

3 | Conclusions

Our work presents a material system in which an out-of-plane magnetic state is realized in a strongly spin–orbit coupled oxide via structural engineering. In contrast to the commonly observed in-plane magnetism in SIO (111) films, we show that a distinct magnetic anisotropy arises when the bulk monoclinic SIO phase is strained to an STO (111) substrate. This strain stabilizes a hexagonal, twinned superstructure featuring coexisting face- and corner-shared IrO_6 octahedra, providing a new platform for engineering spin orientation in 5d transition-metal oxides.

The emergence of ferromagnetism is confirmed spectroscopically by XMCD. DFT + U calculations show that the underlying main mechanism is a Stoner instability driven by a large DOS at E_F, originating from the combined existence of corner- and face-shared octahedra. We argue that the shortened Ir-Ir distance in the interfaces with the face-shared octahedra weakens the effective SOC and enhances the DOS to promote Stoner ferromagnetism. The magnetic moment is estimated to be as small as ~0.03 μB. We expect that the magnetic moment can be further enhanced and tuned by engineering the DOS to enhance $N(E_F)$ through strain imposed by suitable substrates and electrostatic gating.

The strong SOC in this ferromagnetic compound generates a Berry curvature as evidenced by the pronounced AHE observed between 10 and 20 K without hysteresis. Band structure calculations further indicate the existence of Weyl points close to the Fermi energy, suggesting that the material may host a ferromagnetic Weyl semimetal phase.

In spin-orbitronic devices, the SOC is a crucial ingredient both for realizing the spin Hall effect and for manipulating the spin orientation by heterointerfacing with ferromagnets. In this context, our results on SIO(111) films are particularly compelling as they integrate strong SOC and ferromagnetism within the

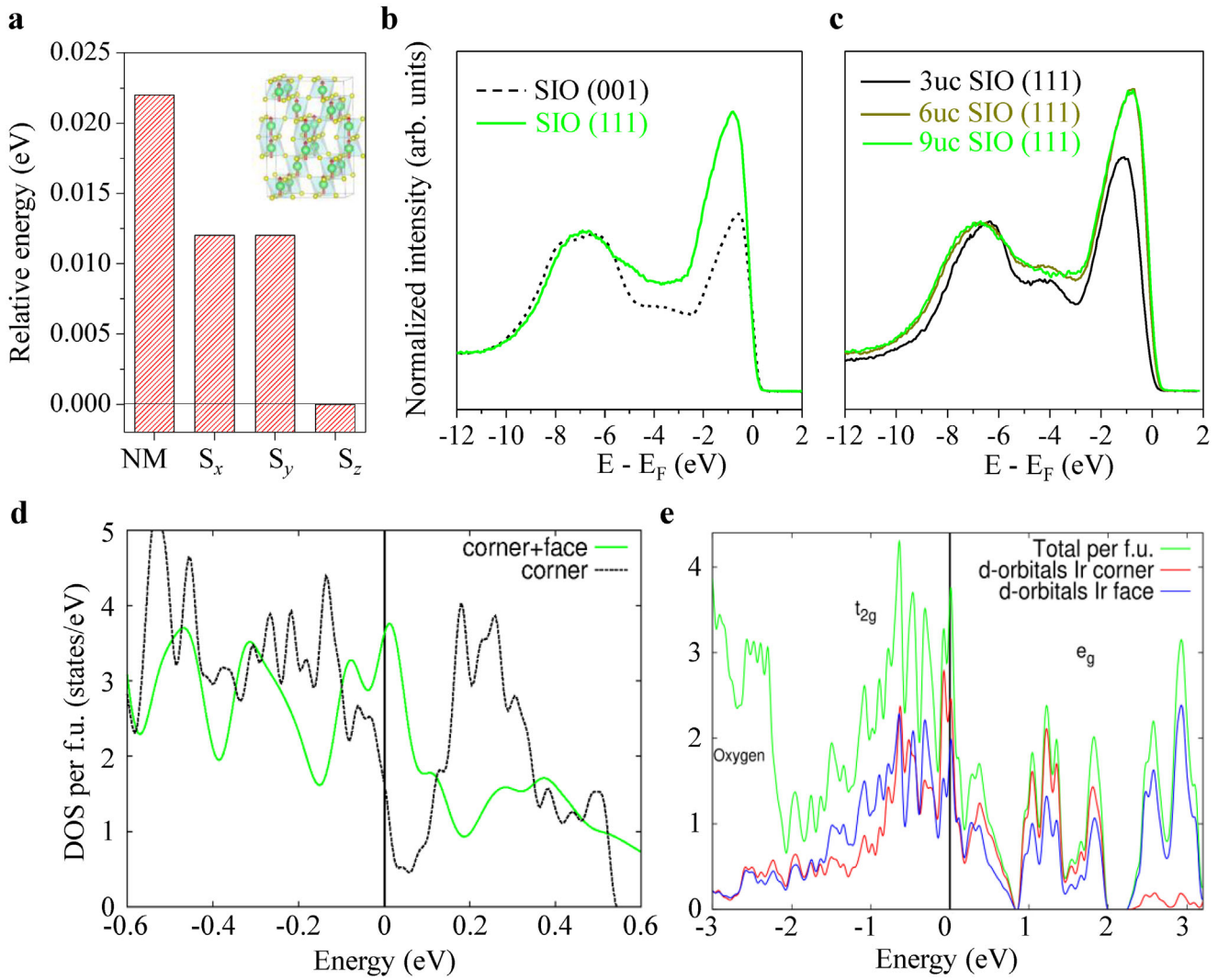

FIGURE 4 | Electronic structure of SIO (001) and (111) films from DFT + U and XPS. (a) Ground state energies of non-magnetic state (NM) and for spin orientations along x, y, and z axes (S_x, S_y, and S_z). The energies are referred to the energy of the S_z state. (b) Angle-integrated valence band spectra of a SIO (001) film with a thickness of 10 uc (black dashed line) and a SIO (111) film with a thickness of 9 uc (green solid line) using X-ray photoelectron spectroscopy (Al Kα = 1486.6 eV). (c) Angle-integrated valence band spectra of SIO (111) films with different thicknesses (3, 6, and 9 uc). (d), DFT + U density of states for SIO (001) and (111) films, depicted by black dashed and solid green lines, respectively. In the SIO (001) film, only corner-shared octahedra are present, while the SIO (111) film comprises a combination of corner- and face-shared octahedra. (e), Total Ir 5d density of states and decomposition into partial density of states for Ir in corner- and face-shared octahedra.

same material system. When incorporated into all-oxide architectures, SIO(111) layers have the potential to serve as an essential functional building block for spin-orbitronic devices, marking an important step forward in both fundamental research and the development of next-generation oxide electronics.

4 | Experimental Section/Methods

4.1 | Growth of SIO Thin Films and X-Ray Diffraction

The pellets were prepared by stoichiometrically mixing $SrCO_3$ (99.9%) and IrO_2 (99.9%) powder (Sigma-Aldrich) and applying high pressure to obtain disk-shaped pellets with a diameter of 1 inch. The pellets were calcinated at 850°C for 12 h under an oxygen flow of 0.5 L/min. After calcination, the pellets were grounded to a fine powder again and pressed and calcinated as before to obtain the final targets for pulsed-laser deposition. To prepare STO substrates (CrysTec GmbH) with Ti termination, the substrates were successively cleaned with acetone, isopropanol, and deionized water and then immersed in buffered hydrofluoric acid (1:6) for 30 s. The STO substrates then were then heated at 1000°C for 3 h in an oxygen flow of 0.5 L per minute. SIO thin films were deposited on Ti-terminated STO (111) and (001) substrates by pulsed laser deposition using a KrF excimer laser (λ = 248 nm). The substrate temperature during film growth was held at 600°C (STO (111)) and 680°C (STO (001)) in an oxygen environment of 0.08 mbar. Laser fluence and repetition rates were set to ~2 J cm^{-2} and 3 Hz, respectively. All films were in situ cooled down to room temperature at a rate of 50°C min^{-1} in an oxygen atmosphere of 0.08 mbar. The *c*-axis lattice parameters of

the as-grown SIO thin films were characterized using a four-circle X-ray diffractometer (Bruker D8 Discovery) with Cu $K_{\alpha 1}$ radiation.

4.2 | X-Ray Photoelectron Spectroscopy

Angle-integrated valence band spectra of SIO (001) and (111) films were recorded in situ at room temperature by X-ray photoelectron spectroscopy with an Al Kα source (1486.6 eV) (Scienta Omicron GmbH). The spectra were taken in normal emission geometry.

4.3 | Transmission Electron Microscopy (TEM)

High-resolution scanning TEM (HR-STEM) was carried out using a TF Titan^3 80–300 probe-corrected instrument (Thermo Fisher Scientific Inc., USA) operated at 300 kV acceleration voltage. Scan images were recorded with a high-angle annular dark-field (HAADF) detector at a camera length of 73 mm (collection angle 80–200 mrad), a probe semi-convergence angle of 21.5 mrad, a pixel size of 12.6 pm, and a dwell time of 6 µs. In order to fit the atom positions of the HAADF-STEM images with pm-scale precision, the coarse positions were first determined using a spatial band-pass filter, that is, the so-called difference of Gaussians (DoG) method [52]. Then, both the higher local contrast of the Ir atoms and their approximate distances were used to distinguish them from the other atomic species. Finally, the precise Ir atom centers were obtained by means of 2D Gaussian peak fitting.

4.4 | Electrical Transport Measurement

Magnetotransport measurements were carried out using a Quantum Design Physical Property Measurement System (PPMS-9T) with resistivity option, by applying an AC current of 10 µA. As-grown samples (5 mm x 5 mm) were mounted on PPMS-sample pucks. Electrical connections in van-der-Pauw geometry were made with Al wires that were bonded directly to the sample surface and to the metal pads of the sample pucks using an ultrasonic wire bonder. A magnetic field was applied perpendicular to the sample surface. Magnetoresistance and Hall measurements were performed from the lowest temperature of 2 K up to 300 K in 20 steps of a logarithmic temperature increase.

4.5 | XAS and XMCD Measurements

X-ray absorption spectroscopy (XAS) and X-ray magnetic circular dichroism (XMCD) measurements at the Ir M_5 edge were carried out at the DEIMOS beamline at the SOLEIL synchrotron facility (France) [40]. All samples were transferred into an ultrahigh vacuum suitcase (base pressure ~10^{-10} mbar) to prevent degradation in air. As the signal, the total electron yield (TEY) was measured with a drain current detector, while the incident X-ray intensity was monitored by the photocurrent of a gold mesh with 25% transmission. A large beam spot size of 800 × 800 µm^2 on the sample was used to avoid radiation damage. All samples were measured in a single sequence with alternating polarizations ($\mu^+\mu^+\mu^-\mu^-\mu^+$), with the initial μ^+ spectrum being excluded from the XMCD analysis. To isolate the XMCD signal, a Shirley background was subtracted to account for the absorption into the free-electron continuum. (Figure S5)

4.6 | Calculation of Electronic Band Structure

DFT calculations were performed using the VASP ab initio simulation package [53], employing the projector-augmented wave (PAW) method [54] within the generalized gradient approximation (GGA). The revised Perdew-Burke-Ernzerhof (PBEsol) [55] functional was used, both with and without the inclusion of spin-orbit coupling (SOC). The plane-wave cutoff energy for expanding the Kohn-Sham orbitals was set to 400 eV. Brillouin-zone integration was carried out using a Monkhorst-Pack [56] k-point mesh of 10 × 6 × 4, centered at the M-point. On-site Hubbard Coulomb repulsion and Hund's exchange were incorporated using the DFT+U method with realistic values which best fit the experimental data of bulk orthorhombic $SrIrO_3$. These electronic parameters were determined to be U = 0.8 eV and $J_H = 0.15U$ [57].

Author Contributions

All authors discussed the results and contributed to the completion of the manuscript. J.S.L. and C.A. wrote the manuscript. Thin film growth was performed by J.S.L. and M.S. Magnetotransport, XPS, and XRD measurements were carried out by J.S.L. XMCD and XAS experiments were conducted by J.S.L. with the assistance of F.C. and P.O. at the SOLEIL-DEIMOS beamline. Theoretical calculations were performed by C.A., A.F., M.C., and G.S. TEM measurements and analyses were conducted by M.K., P.P., D.W., S.P., J.S., and A.L. Angular magnetotransport under high magnetic fields was investigated by N.P., B.M., and L.V. B.B. supervised the TEM and high-field magnetotransport studies. M.S. and R.C. supervised and coordinated the overall project.

Acknowledgements

We gratefully acknowledge funding by the Deutsche Forschungsgemeinschaft (DFG) through Projects No. 461150024 and No. 431448015, through the Collaborative Research Centers SFB 1143 (project C04, project id 247310070) and SFB 1170 (project C08, project id 258499086) as well as the Würzburg–Dresden Cluster of Excellence ct.qmat, EXC 2147 (project id 390858490). We also appreciate financial support by the Bundesministerium für Bildung und Forschung (BMBF) through the project OperandoHAXPES (project number 05K22WW1). L.V. acknowledges support from the French ANR under projects ANR-24-CE92-0021-01 and ANR-23-CPJ1-0158-01, and from the Leibniz Association through the Leibniz Competition. C. A. is supported by the Foundation for Polish Science project "MagTop" No. FENG.02.01-IP.05-0028/23 co-financed by the European Union from the funds of Priority 2 of the European Funds for a Smart EconomyProgram2021–2027 (FENG). C.A. and M.C. acknowledge support from PNRR MUR project PE0000023-NQSTI. A.F. was supported by the Polish National Science Center under Project No. 2020/37/B/ST5/02299. We acknowledge the computing resources and support provided by the computer systems of the Interdisciplinary Centre for Mathematical and Computational Modelling at the University of Warsaw, through Grants No. g911418, No. g91-1419, No. g91-1426, No. g96-1808, and No. g96-1809. XMCD and XAS were performed at the DEIMOS beamline at the SOLEIL Synchrotron facility, France (proposal number: 20230230). We are grateful to the SOLEIL staff for their excellent support. We also gratefully acknowledge Ivan Soldatov and Rudolf Schäfer at the Leibniz Institute for Solid State and Materials Research Dresden for valuable discussions regarding the magnetic domains of the SIO (111) films.

Conflicts of Interest

The authors declare no conflicts of interest.

Data Availability Statement

The data that support the findings of this study are available from the corresponding author upon reasonable request.

References

1. S. Bhatti, R. Sbiaa, A. Hirohata, H. Ohno, S. Fukami, and S. N. Piramanayagam, "Spintronics Based Random Access Memory: a Review," *Materials Today* 20 (2017): 530, https://doi.org/10.1016/j.mattod.2017.07.007.

2. D. D. Awschalom and M. E. Flatte, "Challenges for Semiconductor Spintronics," *Nature Physics* 3 (2007): 153, https://doi.org/10.1038/nphys551.

3. S. D. Bader and S. S. P. Parkin, "Spintronics," *Annual Review of Condensed Matter Physics* 1 (2010): 71–88, https://doi.org/10.1146/annurev-conmatphys-070909-104123.

4. Q. Wang, Y. Gu, C. Chen, F. Pan, and C. Song, "Oxide Spintronics as a Knot of Physics and Chemistry: Recent Progress and Opportunities," *The Journal of Physical Chemistry Letters* 13 (2022): 10065, https://doi.org/10.1021/acs.jpclett.2c02634.

5. F. Trier, P. Noël, J.-V. Kim, J.-P. Attane, L. Vila, and M. Bibes, "Oxide Spin-Orbitronics: Spin–Charge Interconversion and Topological Spin Textures," *Nature Reviews Materials* 7 (2022): 258–274.

6. L. Liu, Q. Qin, W. Lin, et al., "Current-Induced Magnetization Switching in All-Oxide Heterostructures," *Nature Nanotechnology* 14 (2019): 939, https://doi.org/10.1038/s41565-019-0534-7.

7. S. Hu, D.-F. Shao, H. Yang, et al., "Efficient Perpendicular Magnetization Switching by a Magnetic Spin Hall Effect in a Noncollinear Antiferromagnet," *Nature Communications* 13 (2022): 4447, https://doi.org/10.1038/s41467-022-32179-2.

8. K.-W. Kim, B.-G. Park, and K.-J. Lee, "Spin Current and Spin-Orbit Torque Induced by Ferromagnets," *npj Spintronics* 2 (2024): 8.

9. A. Davidson, V. P. Amin, W. S. Aljuaid, P. M. Haney, and X. Fan, "Perspectives of Electrically Generated Spin Currents in Ferromagnetic Materials," *Physics Letters A* 384 (2020): 126228, https://doi.org/10.1016/j.physleta.2019.126228.

10. J. Sinova, S. O. Valenzuela, C. H. Back, and T. Jungwirth, "Spin Hall Effects," *Reviews of Modern Physics* 87 (2015): 1213, https://doi.org/10.1103/RevModPhys.87.1213.

11. Y. Hibino, T. Taniguchi, K. Yakushiji, A. Fukushima, H. Kubota, and S. Yuasa, "Giant Charge-to-Spin Conversion in Ferromagnet via Spin-Orbit Coupling," *Nature Communications* 12 (2021): 6254.

12. M. Aoki, Y. Yin, S. Granville, et al., "Gigantic Anisotropy of Self-Induced Spin-Orbit Torque in Weyl Ferromagnet Co_2 MnGa," *Nano Letters* 23, no. 15 (2023): 6951–6957, https://doi.org/10.1021/acs.nanolett.3c01573.

13. L. Liu, C. Zhou, X. Shu, et al., "Symmetry-Dependent Field-Free Switching of Perpendicular Magnetization," *Nature Nanotechnology* 16 (2021): 277–282, https://doi.org/10.1038/s41565-020-00826-8.

14. Y. J. Chang, C. H. Kim, S.-H. Phark, Y. S. Kim, J. Yu, and T. W. Noh, "Fundamental Thickness Limit of Itinerant Ferromagnetic $SrRuO_3$ Thin Films," *Physical Review Letters* 103 (2009): 057201, https://doi.org/10.1103/PhysRevLett.103.057201.

15. M. Kim and B. I. Kim, "Nature of Itinerant Ferromagnetism of $SrRuO_3$: a DFT+DMFT Study," *Physical Review B* 91 (2015): 205116, https://doi.org/10.1103/PhysRevB.91.205116.

16. Y. Jo, Y. Kim, S. Kim, et al., "Field-Free Spin–Orbit Torque Magnetization Switching in a Single-Phase Ferromagnetic and Spin Hall Oxide," *Nano Letters* 24 (2024): 7100–7107, https://doi.org/10.1021/acs.nanolett.4c01788.

17. A. Biswas, K.-S. Kim, and Y. H. Jeong, "Metal Insulator Transitions in Perovskite $SrIrO_3$ Thin Films," *Journal of Applied Physics* 116 (2014): 213704, https://doi.org/10.1063/1.4903314.

18. D. J. Groenendijk, C. Autieri, J. Girovsky, et al., "Spin-Orbit Semimetal $SrIrO_3$ in the Two-Dimensional Limit," *Physical Review Letters* 119 (2017): 256403, https://doi.org/10.1103/PhysRevLett.119.256403.

19. P. Schütz, D. D. Sante, L. Dudy, et al., "Dimensionality-Driven Metal-Insulator Transition in Spin-Orbit-Coupled SrIrO3," *Physical Review Letter* 119 (2017): 256404.

20. J. Matsuno, K. Ihara, S. Yamamura, et al., "Engineering a Spin-Orbital Magnetic Insulator by Tailoring Superlattices," *Physical Review Letters* 114 (2015): 247209, https://doi.org/10.1103/PhysRevLett.114.247209.

21. J. Liu, X. Zhang, Y. Ji, et al., "Controllable Itinerant Ferromagnetism in Weakly Correlated 5d $SrIrO_3$," *The Journal of Physical Chemistry Letters* 13 (2022): 11946–11954, https://doi.org/10.1021/acs.jpclett.2c03313.

22. G. R. Jeffrey, K.-H. L. Eric, and K. Hae-Young, "Spin-orbit Physcis Giving Rise to Novel Phases in Correlated Systems: Iridates and Related Materials," *Annual Review of Condensed Matter Physics* 7 (2016): 195.

23. T. C. van Thiel, J. Fowlie, C. Autieri, et al., "Coupling Lattice Instabilities across the Interface in Ultrathin Oxide Heterostructures," *ACS Materials Letters* 2 (2020): 389–394, https://doi.org/10.1021/acsmaterialslett.9b00540.

24. G. Cao, V. Durairaj, S. Chikara, L. E. DeLong, S. Parkin, and P. Schlottmann, "Non-Fermi-Liquid Behavior in Nearly Ferromagnetic $SrIrO_3$ Single Crystals," *Physical Review B* 76 (2007): 100402(R), https://doi.org/10.1103/PhysRevB.76.100402.

25. S. Okamoto and D. Xiao, "Transition-Metal Oxide (111) Bilayers," *Journal of the Physical Society of Japan* 87 (2018): 041006, https://doi.org/10.7566/JPSJ.87.041006.

26. T. J. Anderson, S. Ryu, H. Zhou, et al., "Metastable Honeycomb $SrTiO_3/SrIrO_3$ Heterostructures," *Applied Physics Letters* 108 (2016): 151604, https://doi.org/10.1063/1.4947006.

27. X. Zheng, S. Kong, J. Zhu, et al., "Layer-by-Layer Epitaxial Growth of Monoclinic $SrIrO_3$ Thin Films on (111)-Oriented $SrTiO_3$ through Interface Engineering," *Thin Solid Films* 709 (2020): 138119, https://doi.org/10.1016/j.tsf.2020.138119.

28. W. Zhao, M. Gu, D. Xiao, et al., "Tuning the Magnetic Anisotropy in Artificially Layered Mn_3GaN/Mn_3Ga Superlattices," *Physical Review Materials* 8 (2024): 105001, https://doi.org/10.1103/PhysRevMaterials.8.L011401.

29. H. Shilin, L. Meilin, X. Wen, et al., "Emerging Anomalous Hall Effect in (111)-Oriented Artificial Iridate Honeycomb Lattices," *Advanced Functional Materials* 35 (2025): 2414425.

30. T. J. Anderson, H. Zhou, L. Xie, et al., "Interfacial B-site Atomic Configuration in Polar (111) and Non-polar (001) $SrIrO_3/SrTiO_3$ Heterostructures," *APL Mater* 5 (2017): 096110.

31. I. Hallsteinsen, M. Nord, T. Bolstad, et al., "Effect of Polar (111)-Oriented $SrTiO_3$ on Initial Perovskite Growth," *Crystal Growth & Design* 16 (2016): 2357–2362, https://doi.org/10.1021/acs.cgd.6b00143.

32. A. Chanda and R. Mahendiran, "Sharp Steps in Magnetization, Magnetoresistance, and Magnetostriction in $Pr_{0.6}Sr_{0.4}Co_{1-y}Ga_yO_3$," *Applied Physics Letters* 117 (2020): 032402, https://doi.org/10.1063/5.0012581.

33. S. Hurand, A. Jouan, C. Feuillet-Palma, et al., "Field-Effect Control of Superconductivity and Rashba Spin-Orbit Coupling in Top-Gated LaAlO3/SrTiO3 Devices," *Scientific Reports* 5 (2015): 12751.

34. F. Herling, C. Morrison, C. S. Knox, et al., "Spin-Orbit Interaction in InAs/GaSb Heterostructures Quantified by Weak Antilocalization," *Physical Review B* 95 (2017): 155307, https://doi.org/10.1103/PhysRevB.95.155307.

35. Y. Niimi, D. Wei, H. Idzuchi, T. Wakamura, T. Kato, and Y. Otani, "Experimental Verification of Comparability between Spin-Orbit and Spin-Diffusion Lengths," *Physical Review Letters* 110 (2013): 016805, https://doi.org/10.1103/PhysRevLett.110.016805.

36. Y. Cai, H. Wang, D. Yue, D. Tian, and X. Jin, "Spin Diffusion Length in Au Wires and Films Investigated by Weak Antilocalization Measurements," *Applied Physics Letters* 117 (2020): 252401, https://doi.org/10.1063/5.0034886.

37. B. L. Altshuler, A. G. Aronov, and D. E. Khmelnitsky, "Effects of Electron-Electron Collisions with Small Energy Transfers on Quantum Localisation," *Journal of Physics C: Solid State Physics* 15 (1982): 7367–7386, https://doi.org/10.1088/0022-3719/15/36/018.

38. J. M. D. Coey, *Magnetism and Magnetic Materials* (Cambridge Univ. Press, 2009).

39. F. Matsukura, H. Ohno, A. Shen, and Y. Sugawara, "Transport Properties and Origin of Ferromagnetism in (Ga,Mn)As," *Physical Review B* 57 (1998): R2037, https://doi.org/10.1103/PhysRevB.57.R2037.

40. K. Yasuda, A. Tsukazaki, R. Yoshimi, K. S. Takahashi, M. Kawasaki, and Y. Tokura, "Large Unidirectional Magnetoresistance in a Magnetic Topological Insulator," *Physical Review Letters* 117 (2019): 127202, https://doi.org/10.1103/PhysRevLett.117.127202.

41. K. Jaiswal, A. G. Zaitsev, R. Singh, R. Schneider, and D. Fuchs, "Magnetotransport of $SrIrO_3$ Films on (110) $DyScO_3$," *AIP Advances* 9 (2019): 125034, https://doi.org/10.1063/1.5129350.

42. F.-X. Wu, J. Zhou, L. Y. Zhang, et al., "Metal–Insulator Transition in SrIrO3 with Strong Spin–Orbit Interaction," *Journal of Physics-Condensed Matter* 25 (2013): 125604.

43. K. Ueda, R. Kaneko, H. Ishizuka, J. Fujioka, N. Nagaosa, and Y. Tokura, "Spontaneous Hall Effect in the Weyl Semimetal Candidate of All-in All-Out Pyrochlore Iridate," *Nature Communications* 9 (2018): 3032, https://doi.org/10.1038/s41467-018-05530-9.

44. W. J. Kim, T. Oh, J. Song, et al., "Strain Engineering of the Magnetic Multipole Moments and Anomalous Hall Effect in Pyrochlore Iridate Thin Films," *Science Advances* 6 (2020): abb1539, https://doi.org/10.1126/sciadv.abb1539.

45. G. Vértesy, I. Tomáš, L. Půst, and J. Pačes, "Temperature Dependence of Domain-Wall Coercive Field in Magnetic Garnet Films," *Journal of Applied Physics* 71 (1992): 3462–3466.

46. N. Nagaosa, J. Sinova, S. Onoda, A. H. MacDonald, and N. P. Ong, "Anomalous Hall Effect," *Reviews of Modern Physics* 82 (2010): 1539–1592, https://doi.org/10.1103/RevModPhys.82.1539.

47. P. Ohresser, E. Otero, F. Choueikani, et al., "DEIMOS: a Beamline Dedicated to Dichroism Measurements in the 350–2500 eV Energy Range," *Review of Scientific Instruments* 85 (2014): 013106, https://doi.org/10.1063/1.4861191.

48. S. S. Gupta, J. A. Bradley, M. W. Haverkort, G. T. Seidler, A. Tanaka, and G. A. Sawatzky, "Coexistence of Bound and Virtual-Bound States in Shallow-Core to Valence X-Ray Spectroscopies," *Physical Review B* 84 (2011): 075134, https://doi.org/10.1103/PhysRevB.84.075134.

49. S. M. Butorin, "Localization versus Hybridization of f States in Actinide and Lanthanide Dioxides Probed in Core-Level Photoemission Spectra," *Physical Review B* 112 (2025): 125118, https://doi.org/10.1103/8x4b-6651.

50. C.-K. Duan, M. F. Reid, and G. Ruan, "A Simple Model for the f–d Transition of Actinide and Heavy Lanthanide Ions in Crystals," *Current Applied Physics* 6 (2006): 359–362, https://doi.org/10.1016/j.cap.2005.11.019.

51. M. Ye, H.-S. Kim, J.-W. Kim, et al., "Covalency-driven Collapse of Strong Spin-Orbit Coupling in Face-Sharing Iridium Octahedra," *Physical Review B* 98 (2018): 201105(R), https://doi.org/10.1103/PhysRevB.98.201105.

52. F. Akram, M. A. Garcia, and D. Puig, "Active Contours Driven by Difference of Gaussians," *Scientific Reports* 7 (2017): 14984, https://doi.org/10.1038/s41598-017-14502-w.

53. G. Kresse and D. Joubert, "From Ultrasoft Pseudopotentials to the Projector Augmented-Wave Method," *Physical Review B* 59 (1999): 1758–1775, https://doi.org/10.1103/PhysRevB.59.1758.

54. P. E. Blöchl, "Projector Augmented-Wave Method," *Physical Review B* 50 (1994): 17953.

55. J. P. Perdew, A. Ruzsinszky, G. I. Csonka, et al., "Restoring the Density-Gradient Expansion for Exchange in Solids and Surfaces," *Physical Review Letters* 100 (2008): 136406, https://doi.org/10.1103/PhysRevLett.100.136406.

56. J. D. Pack and H. J. Monkhorst, ""Special Points for Brillouin-Zone Integrations"—A Reply," *Physical Review B* 16 (1977): 1748–1749, https://doi.org/10.1103/PhysRevB.16.1748.

57. N. Manca, D. J. Groenendijk, I. Pallecchi, et al., "Balanced Electron-Hole Transport in Spin-Orbit Semimetal $SrIrO_3$ Heterostructures," *Physical Review B* 97 (2018): 081105, https://doi.org/10.1103/PhysRevB.97.081105.

Supporting Information

Additional supporting information can be found online in the Supporting Information section.

Supporting File: adfm74409-sup-0001-SuppMat.docx.